Stojičkov, M., Zlatar, M., Mazzeo, P. P., Bacchi, A., Radanović, D., Stevanović, N., Jevtović, M., Novaković, I., Anđelković, K., Sladić, D., Čobeljić, B., Gruden, M. (2023). The interplay between spin states, geometries and biological activity of Fe(III) and Mn(II) complexes with thiosemicarbazone. Polyhedron, 237, 116389.
https://doi.org/10.1016/j.poly.2023.116389

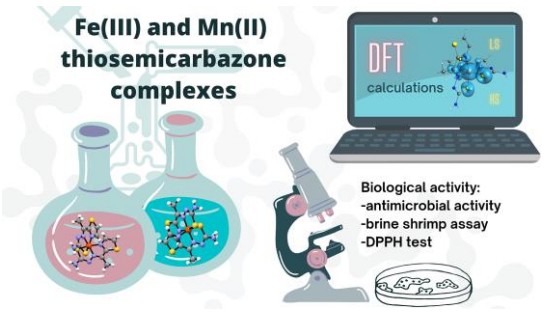

The interplay between spin states, geometries and biological activity of Fe(III) and Mn(II) complexes with thiosemicarbazone

Marko Stojičkov [a], Matija Zlatar [b,*], Paolo Pio Mazzeo [c,d], Alessia Bacchi [c,d], Dušanka Radovanović [b], Nevena Stevanović [a], Mima Jevtović [e], Irena Novaković [b], Katarina Anđelković [a], Dušan Sladić [a], Božidar Čobeljić [a] and Maja Gruden [a,*]

[a]*University of Belgrade - Faculty of Chemistry, Studentski trg 12–16, 11000 Belgrade, Serbia.*
[b]*University of Belgrade - Institute of Chemistry, Technology and Metallurgy, Njegoševa 12, 11000 Belgrade, Serbia.*
[c]*Dipartimento di Scienze Chimiche, della Vita e della Sostenibilità Ambientale, Università degli Studi di Parma, Viale delle Scienze, 17A, 43124 Parma, Italy.*
[d]*Biopharmanet-TEC, Università Degli Studi di Parma, via Parco Area delle Scienze 27/A, Parma, 43124, Italy.*
[e]*Innovation Centre of Faculty of Chemistry, Studentski Trg 12-16, 11000 Belgrade, Serbia*

ABSTRACT

Fe(III) and Mn(II) complexes with condensation product of thiosemicarbazide and 2-acetylthiazole (H**L**[1], (*E*)-2-(1-(thiazol-2-yl)ethylidene)hydrazine-1-carbothioamide) have been synthesized and characterized by single-crystal X-ray diffraction, IR spectroscopy, and elemental analysis. In both complexes, the thiosemicarbazone ligand is coordinated in deprotonated form through the NNS donor set of atoms. However, while Fe(III) complex is in the doublet ground state with distorted octahedral geometry, the coordination environment around Mn(II) is distorted trigonal-prismatic, and the sextet state is found to be the ground state. DFT calculations were performed to rationalize spin state preferences, and continuous shape measure describes the deviation from ideal six-coordinated polyhedral geometries in the ground and excited states. Antimicrobial activity (against a panel of Gram-negative and Gram-positive bacteria, two yeast, and one fungal strain), brine shrimp assay, and DPPH radical scavenging activity of both complexes were evaluated, and these results relate to the electronic structure of the complexes.

Keywords: Schiff base, X-ray diffraction, DFT calculations, spin states, Antimicrobial activity.

1. Introduction

Interpreting and predicting the electronic and magnetic properties of transition metal ions is one of the main challenges in coordination chemistry because all the properties of

* Corresponding authors:
Maja Gruden: gmaja@chem.bg.ac.rs
Matija Zlatar: matija.zlatar@ihtm.bg.ac.rs

complexes with transition metals are inherently related to their electronic structure. Hexacoordinated transition metal complexes are predominantly in octahedral (OC-6) or trigonal-prismatic (TRP-6) geometry. In the trigonal-prismatic environment, the d orbitals are split into three sets (a_1, $2e'$, e''), while in the octahedral geometry, they are split into two groups (t_{2g}, e_g) [1,2]. The characteristic feature of transition metal ions is that they have partially filled d orbitals. The electrons can be arranged differently depending on the central metal ion, the ligands bound to it, and the symmetry of the environment. In a hexacoordinated environment, electrons can be distributed in at least two ways: with a maximum number of unpaired electrons, leading to the high spin (HS) state, or with none or minimal numbers of unpaired electrons – giving the low spin (LS) state. In the case of d^5 ions, irrespective of the symmetry of coordination geometry (OC-6 or TPR-6), two types of spin ground states can be observed: low-spin state with one (S = 1/2) and high-spin state with five unpaired electrons (S = 5/2) [3]. It has been long recognized that having a different number of unpaired electrons (i.e., different spin ground states) directly affects the structure, magnetism, and reactivity of molecules [4]. Bearing that in mind, knowledge of electron distribution could also be relevant in explaining their biological behavior.

In recent decades thiosemicarbazones and their metal complexes have received considerable attention due to their variable bonding properties [5–7], structural diversity [8,9], and a broad spectrum of potentially beneficial biological properties [10–12] that can differ from those of either ligands or the metal ions [13–15]. In many cases, metal complexes exhibit enhanced activity [16]**.**

Herein, we present a thorough study, both experimental and computational (DFT), on Fe(III) and Mn(II) complexes with thiosemicarbazone ligand. Both complexes have the same d^5 electronic configuration, and we will investigate differences in their geometries, spin states, electronic distribution, nature of bonding, and interrelation between those factors. Furthermore, we tried to rationalize their biological activity by means of the electronic structure of the complexes and their geometries.

2. Experimental

2.1. Materials and methods

2-Acetylthiazole (99%) was obtained from Acros, thiosemicarbazide (99%) from Sigma Aldrich, $MnCl_2 \cdot 4H2O$ from Kemika d. d. (Zagreb, Croatia) and $Fe(BF_4)_2 \cdot 6H_2O$ from Sigma-Aldrich. IR spectra were recorded using a Nicolet 6700 FT-IR spectrophotometer using the ATR technique in the region 4000–400 cm−1 (vs – very strong, s – strong, m – medium, and w – weak). Elemental analyses (C, H, and N) were performed by standard micro-methods using an ELEMENTARVario ELIII C. H.N.S.O analyzer. Magnetic measurements were performed at 25°C by Evans' method using an MSBMK1 balance

(Sherwood Scientific Ltd.) with $Hg[Co(SCN)_4]$ as calibrant; diamagnetic corrections were calculated from Pascal's constants.

*2.2. Synthesis of (*E*)-2-(1-(thiazol-2-yl)ethylidene)hydrazine-1-carbothioamide (H**L**^{1})*

2-acetylthiazole (1.040 mL, 10 mmol) was dissolved in water (20 mL), and solid thiosemicarbazide (0.911 g, 10 mmol) was added. The reaction mixture was acidified with 3-4 drops of 2 M HCl and refluxed for 3h. After cooling to room temperature, a white precipitate was obtained. Yield: 1.842 g (92%). IR (ATR, cm^{-1}): 3435.8 (s), 3248.0 (s), 3188.5 (s), 3099.1 (m), 3070.6 (m), 2983.0 (m), 2065.7 (w), 1647.5 (w), 1589.3 (s), 1510.0 (s), 1481.6 (s), 1452.4 (m), 1425.4 (s), 1365.2 (m), 1281.8 (m), 1166.1 (m), 1106.7 (m), 1068.6 (m), 1039.2 (m), 958.0 (w), 881.0 (w), 846.6 (w), 754.6 (w), 711.9 (w), 637.7 (w). Anal. Calcd. (%) for $C_6H_8N_4S_2$: C, 35.98; H, 4.03; N, 27.98; S, 32.02. Found (%): C, 35.74; H, 4.26; N, 27.88; S, 31.98. ^{1}H-NMR (400 MHz, DMSO-d_6), δ (ppm): 2.43 (s, 3H, C1-H), 7.80 (d, 1H, C4-H), 7.89 (d, 1H, C5-H), 7.69; 8.53 (s, NH_2), 10.67(s, 1H, NH). ^{13}C-NMR (125 MHz, DMSO-d_6), δ (ppm): 14.1 (C1), 123.1 (C4), 144.7 (C2), 143.7 (C5), 167.5 (C3), 179.4 (C6).

*2.3. Synthesis of complex [Fe(**L**^{1})$_2$]BF_4H_2O (**1**)*

Ligand H**L**^{1} (0.040 g, 0.20 mmol) was dissolved in MeOH (20 mL), and solid $Fe(BF_4)_2{\cdot}6H_2O$ (0.069 g, 0.20 mmol) was added. The mixture was refluxed for 2h. After slow evaporation of solvent at room temperature after two weeks, brown crystals were obtained. Yield: 0.080 g (72 %). Anal. Calcd. (%) for $C_{12}H_{18}BF_4FeN_8OS_4$: C, 25.68; H, 3.23; N, 19.97; S, 22.85. Found (%): C, 25.75; H, 3.27; N, 20.0; S, 22.65. IR (ATR, cm^{-1}): 3606.6 (w), 3458.5 (m), 3410.2 (m), 3287.9 (s), 3184.2 (s), 1626.8 (s), 1610.3 (s), 1542.2 (m), 1503.7 (s), 1464.0 (s), 1385.1 (s), 1335.7 (s), 1303.9 (s), 1206.7 (m), 1165.1 (s), 1055.4 (s), 892.3 (m), 795.8 (w), 779.9 (m), 741.4 (m), 706.5 (w), 682.9 (w), 655.0 (w), 611.5 (w), 521.1 (w), 478.1 (w). μ_{eff} (297 K) = 1.95 μ_B.

*2.4. Synthesis of complex [Mn(**L**^{1})$_2$] (**2**)*

Ligand H**L**^{1} (0.040 g, 0.20 mmol) was dissolved in a solvent mixture of MeOH/H_2O (20/5 mL), and solid $MnCl_2{\cdot}4H_2O$ (0.039 g, 0.20 mmol) was added. After the complete dissolution of $MnCl_2{\cdot}4H_2O$ in the reaction mixture, NaN_3 (0.052 g, 0.80 mmol) dissolved in water (5 mL) was added. The mixture was refluxed for 2 h. After one week of slow evaporation of the solvent in the refrigerator, yellow crystals were obtained. Yield: 70 mg (77 %). Calcd. (%) for $C_{19}H_{32}MnN_{12}O_2S_6$: C, 32.24; H, 4.56; N, 23.75; S, 27.18. Found (%): C, 32.27; H, 4.60; N, 23.80; S, 27.19. IR (ATR, cm^{-1}): 3491.7 (w), 3467.7 (w), 3361.0 (m), 3272.0 (m), 3127.2 (m), 1618.1 (s), 1574.1 (w), 1555.6 (m), 1488.6 (m), 1421.1 (s),

1375.3 (s), 1292.3 (s), 1187.5 (s), 1151.3 (s), 1093.9 (s), 1020.3 (m), 878.0 (m), 781.2 (m), 718.0 (m), 678.9 (m), 644.2 (w), 562.1 (w), 545.6 (w). μ_{eff} (297 K) = 5.73 μ_B.

2.5. X-ray crystallography

SCXRD analyses were performed on selected single crystal samples on a Bruker D8 Venture diffractometer equipped with a kappa goniometer and an Oxford cryostream. Low-temperature data collections were performed under nitrogen flux. Microfocused MoKα radiation (λ = 0.71073 Å) was used for **1** and **2**. All the structures were solved by direct methods using SHELXT [17] and refined by full-matrix least-squares on all F^2 using SHELXL [18] as implemented in Olex2 [19] using anisotropic thermal displacement parameters for all nonhydrogen atoms (see **Figs. S1−S2** for ORTEP diagrams). **Table S1** reports crystal data collection parameters and refinement results. CCDC 2226697-2226698 contains the supplementary crystallographic data for this paper. These data can be obtained free of charge *via* www.ccdc.cam.ac.uk/data_request/cif or by emailing data_request@ccdc.cam.ac.uk, or by contacting The Cambridge Crystallographic Data Centre, 12 Union Road, Cambridge CB2 1EZ, UK; fax: +44 1223 336033.

2.6. Computational details

All DFT calculations have been performed with the ADF[20,21] engine in Amsterdam Modeling Suite (version 2022.102) [22]. Relativistic effects were considered in all calculations with the zeroth-order regular approximation to the Dirac Hamiltonian in the scalar relativistic formulation [23]. All calculations were performed with an increased numerical quality ("numericalquality Good" in ADF). Before single-point calculations on the complexes from the X-ray structures, the positions of hydrogen atoms were optimized in experimental supramolecular structures using BP86 functional [24–26] with Grimme's third-generation dispersion energy correction [27] and Becke-Johnson damping [28], and DZP basis set on all atoms (in the case of Fe(III) complex: $[Fe^{III}(\mathbf{L^1})_2]^+$-- $[Fe^{III}(\mathbf{L^1})_2]BF_4H_20$-- $[Fe^{III}(\mathbf{L^1})_2]^+$; in the case of Mn(II) complex: $[Mn^{II}(\mathbf{L^1})_2]$-- $[Mn^{II}(\mathbf{L^1})_2]$). The Fast Inertial Relaxation Engine [29] based optimizer in Cartesian coordinates was used for hydrogen optimization. For energies, single-point calculations on complex units ($[Fe^{III}(\mathbf{L^1})_2]^+$ and $[Mn^{II}(\mathbf{L^1})_2]$) have been performed in unrestricted formalism in low-spin (2S+1=1), intermediate spin (IS) (2S+1=4), and high-spin (2S+1=6) states. Both crystallographically independent complex units were considered in Mn(II) case. In these calculations, all-electron triple-zeta Slater-type orbitals plus one polarization function (TZP) basis set were used for all atoms. Several density functional approximations were employed, namely OPBE [30], OLYP [31–34], B97-D [35], SSB-D [36], and B3LYP* [37]. The LibXC library [38] was used for B97-D and SSB-D calculations. Geometry optimizations with the Quasi-Newton method and delocalized coordinates [39] were

performed at the same levels of theory for both low-spin and high-spin states of $Fe^{III}(\mathbf{L^1})_2]^+$and $[Mn^{II}(\mathbf{L^1})_2]$. Spin densities, the difference between alpha and beta electron densities, were represented as 0.005 a.u. colored isosurfaces, where the light-blue color represents the excess of alpha spin, while the red color represents the excess of beta spin. These plots were made with ADF GUI. Nalewajski-Mrozek ("type 3" in ADF) [40] bond orders were computed for both low-spin and high-spin states of $Fe^{III}(\mathbf{L^1})_2]^+$and $[Mn^{II}(\mathbf{L^1})_2]$ at X-ray geometries at B97-D/TZP and SSB-D/TZP levels of theory.

To check the influence of solvation, single-point calculations on X-ray structures and geometry optimizations were performed at B97-D/TZP and SSB-D/TZP levels of theory and the COSMO solvation model [41,42], as implemented in ADF [43], with DMSO as the solvent.

The Cartesian coordinates of all the optimized structures are available in the ESI.

2.7. Antimicrobial activity

Antimicrobial activity was tested against a panel of microorganisms, including: gram-negative bacteria *Escherichia coli* (ATCC 25922), *Pseudomonas aeruginosa* (ATCC 9027), *Proteus hauseri* (ATCC 13315), *Klebsiella pneumoniae* (ATCC 10031), *Salmonella enterica* subsp. enterica serovar Enteritidis (ATCC 13076), gram-positive bacteria *Staphylococcus aureus* (ATCC 6538), *Bacillus subtilis* (ATCC 6633), *Clostridium sporogenes* (ATCC 19404), *Kocuria rhizophila* (ATCC 9341), *Micrococcus luteus* (ATCC 10240), yeasts *Candida albicans* (ATCC 10231), *Saccharomyces cerevisiae* (ATCC 9763) and fungal strain *Aspergillus brasiliensis* (ATCC 16404).

Antimicrobial activity was evaluated using the broth microdilution method according to NCCLS [44]. The 96-well plates were prepared by dispensing 100 µl of Mueller–Hinton broth for bacteria and Sabouraud dextrose broth for yeasts and fungi into each well. A 100 µL aliquot from the stock solution of the tested compounds (concentration 10 mg/mL in DMSO) was added to the first row of the plate and double diluted by using a multichannel pipette. The direct colony method was used in the preparation of a suspension of bacteria and yeasts in sterile 0.9 % saline, while the process of preparing the suspension of fungal spores included gentle stripping of spore from agar slants with growing aspergilli into sterile 0.9 % saline. Suspension turbidity evaluation was conducted by comparison with 0.5 McFarland's standard. A 10 µL of diluted bacterial, yeast, or spores suspension was added to each well to give a final concentration of 5×10^5 CFU/mL for bacteria and 5×10^3 CFU/mL for fungi and yeast. Chloramphenicol served as a positive control for bacteria, while amphotericin B served as a positive control for yeasts and fungi.

The inoculated plates were incubated at 37 °C for 24 h for bacteria and at 28 °C for 48 h for the yeasts and fungi. The bacterial growth was visualized by adding 20 µL of 0.5% 2,3,5-triphenyltetrazolium chloride (TTC) aqueous solution [45]. Minimum inhibitory concentration (MIC) was defined as the lowest concentration of the compounds that

inhibited bacterial growth (red-colored pellet at the bottom of the wells after the addition of TTC).

2.8. Brine shrimp assay

About 20 g of commercially purchased lyophilized eggs of *Artemia salina* (Artemia eggs, Dajana, Czech Republic) were put in 0.5 L of tap water, and the air was passed through the suspension by a pump under illumination over a 48-hour incubation period. All tested compounds were dissolved in DMSO, and various amounts (0.01–1 mg) were added to 950 μL of artificial seawater with freshly hatched nauplii. After 24 h illumination at room temperature, the number of dead and surviving nauplii were counted and statistically analyzed. LC_{50} was defined as a concentration of compounds that caused the death of 50% of the nauplii. All samples were done in triplicate, while $K_2Cr_2O_7$ served as a positive control.

2.9. DPPH radical scavenging activity

The 2,2-diphenyl-1-picrylhydrazyl (DPPH) radical scavenging activity was determined by the method of Blois [46]. Commercially available free radical DPPH was dissolved in methanol at a concentration of 6.58×10^{-5} M, while tested compounds were dissolved in DMSO. Into a 96-well microplate, 50 μL solutions of the tested compounds at concentrations range 20 to 0.01 mg/mL were loaded (50 μL DMSO in control), and 100 μL of DPPH solution was added. Samples were incubated for 30 minutes in the dark at room temperature, after which absorbance was measured at 517 nm. All the measurements were performed in triplicate, and the scavenging activity of the tested derivatives was calculated as:

$$\text{Scavenging activity (\%)} = 100\times(A_{control} - (A_{sample} - A_0))/A_{control}$$

where $A_{control}$ and A_{sample} refer to the absorbance of DPPH in the control solution and sample, respectively, while A_0 refers to the absorbance of the solutions of compounds because of their color.

The IC_{50} was defined as the antioxidant concentration necessary to decrease the amount of the initial DPPH radical by 50 % and was calculated from the plotted graph of scavenging activities against the concentrations of the tested compounds. Ascorbic acid was employed as the positive control (concentrations from 50 to 500 μg mL^{-1}).

3. Results and discussion

3.1. Synthesis

The H**L**^{1} ligand, (*E*)-2-(1-(thiazol-2-yl)ethylidene)hydrazine-1-carbothioamide, was obtained from the condensation reaction of thiosemicarbazide and 2-acetylthiazole in water (Scheme 1). The reaction of the ligand H**L**^{1} with $Fe(BF_4)_2 \cdot 6H_2O$ in a molar ratio 1:1 in methanol results in the formation of bis Fe(III) complex (**1**) with composition $[Fe(\mathbf{L}^{1})_2]BF_4 \cdot H_2O$ (Scheme 1). The reaction of the H**L**^{1} ligand with the metal salt $MnCl_2 \cdot 4H_2O$ in a molar ratio 1:1 in methanol/water mixture results in the formation of bis Mn(II) complex (**2**) with composition $[Mn\mathbf{L}^{1}_2]$ (Scheme 1). In both complexes, deprotonated hydrazone ligands were coordinated in a tridentate fashion through NNS donor set atoms.

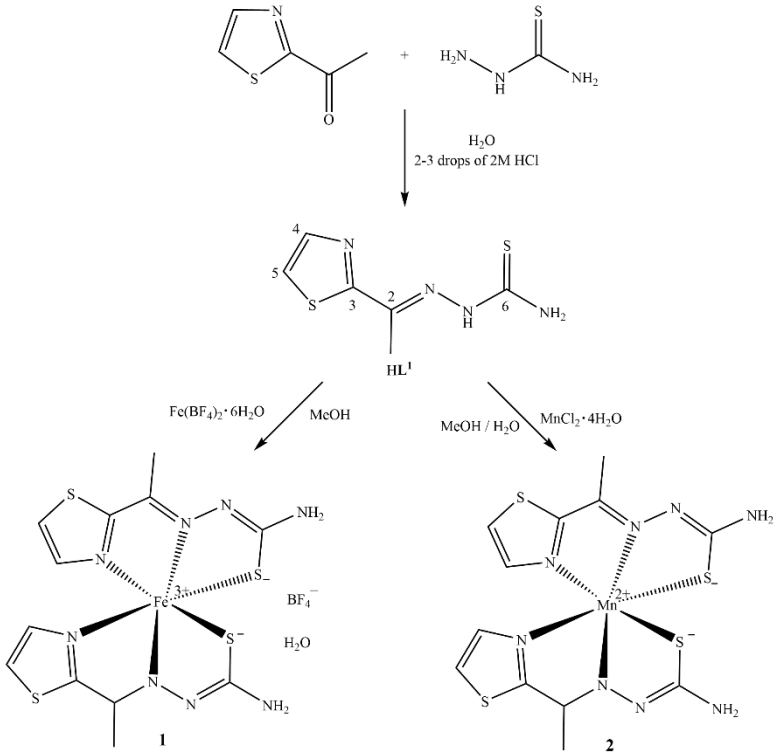

Scheme 1. Synthesis of the ligand (H**L**^{1}), $[Fe(\mathbf{L}^{1})_2]BF_4 \cdot H_2O$ (**1**) and $[Mn\mathbf{L}^{1}_2]$ (**2**) complexes.

3.2. IR spectra

The IR spectroscopy data confirm that the H**L**^{1} ligand is coordinated in a deprotonated form since the ν(N–H) band, at 3435.8 cm^{-1} is absent in the spectrum of complexes **1** and **2**. In the IR spectrum of complex **1** bands at 1464.0 and 892.3 cm^{-1} corresponds to ν(C = S) + ν(C = N) and ν(C = S) + γ(CH), respectively, while in the spectrum of non-coordinated H**L**^{1} ligand ν(C = S) + ν(C = N) and ν(C = S) + γ(CH) bands appeared at 1481.6 and 1068.6 cm^{-1}.

Similarly, in the IR spectrum of complex **2** bands at 1488 and 878 cm^{-1} corresponds to ν(C = S) + ν(C = N) and ν(C = S) + γ(CH), respectively.

*3.3. Crystal structures of [Fe($\mathbf{L^1}$)$_2$]BF_4·H_2O (**1**) and [Mn($\mathbf{L^1}$)$_2$] (**2**) complexes*

The structures of **1** and **2** are depicted in **Figs. 1** and **2**, respectively, where the numbering schemes adopted for the respective atoms are also given. Selected bond lengths and angles are shown in **Table S2**. The Fe(III) and Mn(II) ions with $\mathbf{L^1}$ form six-coordinate complexes [Fe($\mathbf{L^1}$)$_2$]BF_4·H_2O (**1**) and [Mn($\mathbf{L^1}$)$_2$] (**2**) in which two deprotonated ligand molecules coordinate in tridentate fashion to the metallic center through thiazole and imine nitrogen atoms and thiolate sulfur atom.

*3.3.1. Crystal structure of complex **1***

Complex **1** crystallizes in the orthorhombic crystal system with space group *Pbca*. The asymmetric unit (asu) of **1** consists of a complex cation [Fe($\mathbf{L^1}$)$_2$]$^+$, BF_4^- counter anion, and one solvent water molecule. Two deprotonated ligand molecules $\mathbf{L^1}$ coordinate the Fe(III) ion in a *mer* arrangement, forming a distorted octahedral complex by chelation through NNS sets of donor atoms. The mean deviation of 12 octahedral bond angles from ideal 90° sums 5.9°. The tridentate coordination of each ligand implies the formation of two fused five-membered chelate rings Fe–N–C–C–N and Fe–N–N–C–S, which are noncoplanar, as indicated by the dihedral angles of 5.3° and 3.2° for the rings fused along Fe1–N7 and Fe1–N3 bonds, respectively. The two chelation planes comprising the atoms S–N–N–Fe are nearly perpendicular. The Fe–L mean bond distances: Fe–$N_{thiazole}$ 1.982 Å, Fe–N_{imine} 1.939 Å, and Fe–$S_{thiolate}$ 2.222 Å are in close agreement with those observed in related low spin Fe(III)-N_4S_2 complexes with thiosemicarbazone ligands [47,48] (**Table S3** in the Supplementary information file). The Fe–$N_{thiazole}$ and Fe–N_{imine} bond distances are slightly longer than the corresponding bonds in [Co($\mathbf{L^1}$)$_2$]$^+$ complexes with the same thiosemicarbazone ligand [15,49] (**Table S4** in the ESI file).

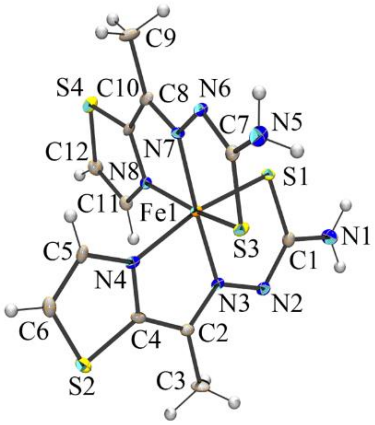

Fig. 1. The ORTEP drawing of [Fe($\mathbf{L^1}$)$_2$]$^+$ complex cation in **1**. Thermal ellipsoids are drawn at the 30% probability level.

The effect of the metal ion size on the molecular organization is observed for the crystals of the [Fe($\mathbf{L^1}$)$_2$]BF_4·H_2O (**1**) and [Co($\mathbf{L^1}$)$_2$]BF_4·H_2O [15] complexes which crystallize in the same space group *Pbca* (No 61) with almost the same lattice parameters. In the crystals of **1,** the cationic units [Fe($\mathbf{L^1}$)$_2$]$^+$ form chains running parallel with [100] direction through the intermolecular hydrogen bonds formed between terminal NH_2 groups serving as hydrogen bond donors and nitrogen atoms from thioamide fragment as acceptors (**Table S5** and **Fig. S1a**). The BF_4^- anions and solvent water molecules mediate the linking of the hydrogen-bonded chains into a layer parallel with the (010) lattice plane through the intermolecular hydrogen bonds involving terminal NH_2 group and thioamide nitrogen from $\mathbf{L^1}$, BF_4^- anion, and a solvent water molecule (**Table S5** and **Fig. S3a**). The neighboring layers are linked through the intermolecular π···π interactions between thiazole rings and N–H···π(thiazole ring) interaction (**Fig. S3b**). Geometric parameters describing π···π and N–H···π interactions are given in **Tables S6** and **S7** in the ESI. However, in the crystal structure of the [Co($\mathbf{L^1}$)$_2$]BF_4·H_2O [15] complex, the cationic units [Co($\mathbf{L^1}$)$_2$]$^+$ self-assemble within a layer parallel with the (001) lattice plane by means of intermolecular hydrogen bonds between terminal NH_2 groups serving as hydrogen bond donors and thiolate sulfur and nitrogen atoms from thioamide fragment as acceptors. BF_4^- anions are settled in between the cationic layers. Similar 2D assembly of the complex cations [Co($\mathbf{L^1}$)$_2$]$^+$ generated by intermolecular hydrogen bonding was also observed in the crystal structure of the [Co($\mathbf{L^1}$)$_2$]$_2$[Co$(NCS)_4$]·$2H_2O$ complex [49].

*3.3.2. Crystal structure of complex **2***

Complex **2** crystallizes in the triclinic crystal system with space group $P\bar{1}$. The asymmetric unit (asu) of **2** consists of two crystallographically independent [Mn($\mathbf{L^1}$)$_2$] complex molecules. The Mn(II) ion is hexacoordinated with two tridentate ligands $\mathbf{L^1}$ through NNS sets of donor atoms. The geometry around the Mn1 and Mn2 is described as a distorted trigonal prism (TPR-6) with the twist angles Φ of 27.5° and 21.3° (mean values) being calculated applying "method 1" reported in ref. [50] for the atom pairs S1N3, S3N4, N7N8 and S7N15, S5N16, N11N12, respectively. The tridentate coordination of each ligand implies the formation of two fused five-membered chelate rings Mn–N–C–C–N and Mn–N–N–C–S, which show significant deviation from planarity, as indicated by the dihedral angles of 14.0°, 8.8°, 12.5° and 16.0° for the rings fused along Mn1–N3, Mn1–N7, Mn2–N11 and Mn2–N15 bonds, respectively. The Mn–L mean bond distances are: Mn–$N_{thiazole}$ 2.271 Å, Mn–N_{imine} 2.2585 Å, and Mn–$S_{thiolate}$ 2.5205 Å (**Table S4** in the ESI). The Mn–N_{imine} and Mn–$S_{thiolate}$ bond distances are slightly longer than the corresponding bonds observed in [Zn($\mathbf{L^1}$)$_2$] complex, while the mean M–$N_{thiazole}$ (M = Mn(II) and Zn(II)) bonds are comparable in length (**Table S4**).

In the crystals of complex **2**, neutral complex species [Mn($\mathbf{L^1}$)$_2$] self-assemble within a layer parallel with the (010) lattice plane through intermolecular N–H···N and N–H···S hydrogen bonds (**Table S8** and **Fig. S4**). The formation of 2D assembly of [Mn($\mathbf{L^1}$)$_2$] is

supported by π···π interaction between thiazole rings and N–H···π(thiazole ring) interactions (**Tables S9** and **S10** in the ESI). Crystallographic programs ORTEP-3 for Windows [51] and Mercury [52] were used to prepare drawings.

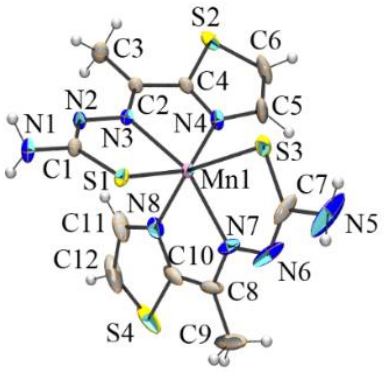

Fig. 2. The ORTEP drawing of one of the two crystallographically independent [Mn(**L**^{1})$_2$] complex molecules extracted from the crystal of **2**. Thermal ellipsoids are drawn at the 30% probability level.

3.4. Magnetic measurements

In this work, we have synthesized and characterized Fe(III) and Mn(II) complexes with the same thiosemicarbazone ligand. Both complexes have the same d^5 configuration of the central metal ion. Octahedral thiosemicarbazone Fe(III) complex was found to be paramagnetic and in the low spin ground state (1.95 μ_B), in accordance with previously investigated magnetic moment values in the range of 1.60–2.33 μ_B [53–57] (except for the cases in which a high spin center, identified as tetrachloroferrate(III) anion, can be found in the structure of the complex [57]). Mn(II) complex possesses trigonal prismatic geometry and high spin ground state with the value of magnetic susceptibility (5.73 μ_B) that agrees with the values found for similar complexes (5.33–6.55 μ_B [58–61]).

3.5. Computational study

Transition metal ions with partially filled d-shells can exhibit different kinds of spin multiplicity in the ground state, i.e., they have different spin states [62,63]. Herein, we have two complexes with the same electronic configuration and ligand system. Measured effective magnetic moments (1.95 μ_B and 5.73 μ_B for Fe(III) and Mn(II) complexes, respectively) and analysis of the crystal geometries suggest that the two complexes studied in this work have a different number of unpaired electrons. Therefore, we performed the density functional theory (DFT) calculations with different density functional approximations (DFAs) to elucidate the ground spin state, **Table 1**.

Table 1. Relative spin state energies (in kcal/mol) for $[Fe^{III}(\mathbf{L^1})_2]^+$ and $[Mn(\mathbf{L^1})_2]$ at different levels of theory.

	$[Fe^{III}(\mathbf{L^1})_2]^+$		$[Mn^{II}(\mathbf{L^1})_2]$		
Level of theory	E_{HS-LS} (X-ray)[a]	E_{HS-LS} (opt.)[b]	E_{HS-LS}(X-ray1)[a]	E_{HS-LS} (X-ray2)[a]	E_{HS-LS} (opt.)[b]
OPBE/TZP	50.74	18.97	-51.15	-52.99	-0.15
OLYP/TZP	53.75	13.48	-44.11	-46.07	-4.59
B97-D/TZP	50.43	11.40	-46.91	-48.80	-5.41
SSB-D/TZP	43.84	8.57	-49.42	-51.23	-5.76
B3LYP*/TZP	52.53	14.03	-40.45	-42.84	-8.60
B97-D/TZP-COSMO[c]	49.08	11.58	-49.28	-51.24	-6.90
SSB-D/TZP-COSMO[c]	42.62	8.92	-51.20	-53.53	-7.00

[a)] single-point on X-ray geometries; for Mn(II) complex, two crystallographically independent complexes are considered; [b)] geometry optimization; [c)] DMSO as solvent.

It is noteworthy that testing the performance of different DFAs is of utmost importance, as it has been shown that the accuracy of the results strongly depends on the choice of the DFAs [62]. The relative spin state energies were calculated on crystal structures of two crystallographically independent Mn(II) complex units and Fe (III) complex (vertical spin state splittings), but also on optimized geometries ("relaxed").

For Fe(III) complex, the doublet spin state was found to be the ground state, i.e., the LS complex is always, independent of the type of calculation and level of theory, the most stable one. Comparing the vertical spin state energies, calculated on the crystal structure, with results from the optimized ("relaxed") geometries, **Table 1** shows that the energy gap between different spin states decreased. On the other hand, the ground spin states of the Mn(II) complexes are sextet, with five unpaired electrons. The doublet ground state is significantly higher in energy. However, as in the previous case, this difference is smaller in optimized structures and depends on the geometry of obtained minimal energy structure (see below). These results are in accordance with the effective magnetic moment measurements (1.95 μB for Fe(III) complex and 5.73 μB for Mn(II) complex, respectively) that are close to the spin-only values (LS d^5: 1.73 μB; HS d^5: 5.92 μB). Bond distances around the metal center are consistent with these results, as longer bonds are observed for the high-spin complexes (**Tables S11 and S12**).

For the intermediate, quartet, states of the Fe(III) and Mn(II) complexes, vertical and relaxed spin state splittings were calculated for consistency (**Table S13**). Single-point calculations on X-ray geometries showed intermediate spin as the first excited state. However, optimizing the geometries of the quartet states resulted in the most unstable structures for Fe(III) and Mn(II) complexes.

If we look at the spin densities, they also differ (**Fig. 3**). In the manganese complex, ground spin density is located almost exclusively on the metal center and presents the textbook example of the spherical distribution of HS five d electrons (**Fig. 3B**). In the LS Mn(II), there is a spin polarization on neighboring ligator atoms (**Fig. 3E**). In both spin states of the Fe(III) complex, there is a spin delocalization on ligator atoms. In the ground, LS state of Fe(III) spin delocalization is mainly toward Sulphur atoms (**Fig. 3D**). This indicates that covalency is higher in the Fe(III) complex than in the Mn(II) complexes. This

is further confirmed with higher bond orders in Fe(III) complex (**Table 2**). **Table 2** shows that, in general, LS states of both complexes have higher bond order than corresponding HS states. Hence, stronger metal−ligand covalency prefers LS states, as in the case of the ground state of the Fe(III) complex. In Mn(II) complex, Hund's rule of maximum multiplicity is responsible for its HS ground state. This analysis confirms that the ground spin state results from an interplay between these two opposing effects (covalency vs. Hund's rule) [64].

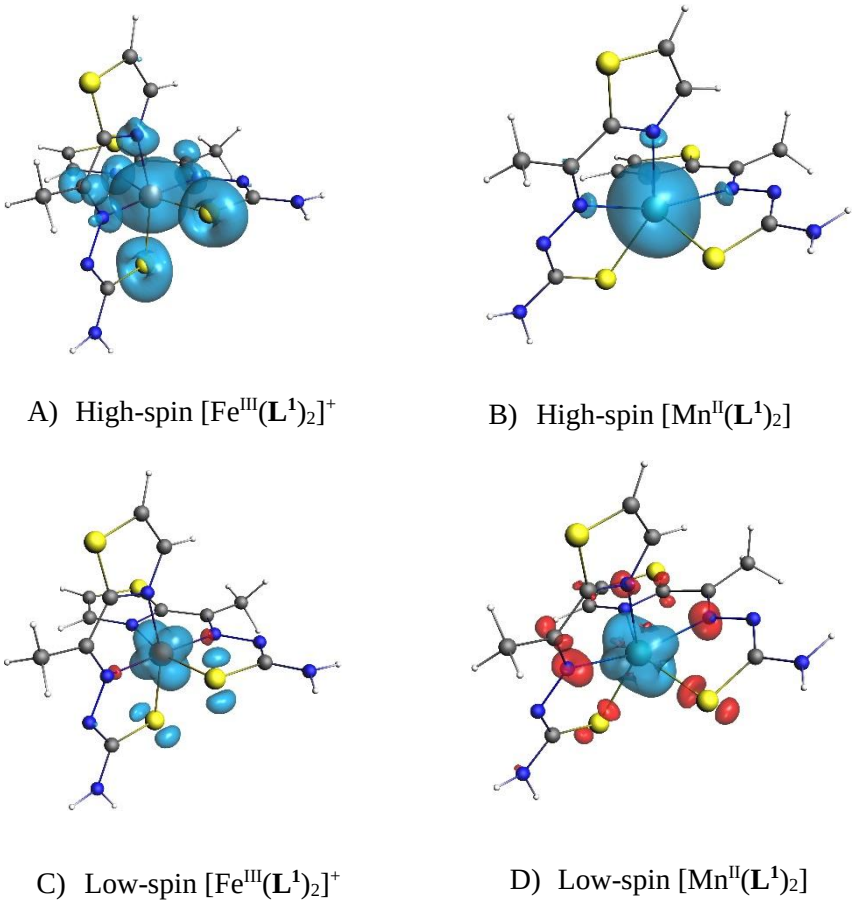

A) High-spin $[Fe^{III}(\mathbf{L^1})_2]^+$ B) High-spin $[Mn^{II}(\mathbf{L^1})_2]$

C) Low-spin $[Fe^{III}(\mathbf{L^1})_2]^+$ D) Low-spin $[Mn^{II}(\mathbf{L^1})_2]$

Fig. 3. Spin densities (the difference between alpha and beta electron densities) calculated at B97-D/TZP level of theory on crystal structures of $[Fe^{III}(\mathbf{L^1})_2]^+$ (A) high-spin; C) low-spin) and $[Mn^{II}(\mathbf{L^1})_2]$ (B) high-spin; D) low-spin). Spin densities were represented as 0.005 a.u. colored isosurfaces, where the light-blue color represents the excess of alpha spin, while the red color represents the excess of beta spin. The ground spin state of $[Fe^{III}(\mathbf{L^1})_2]^+$ is low-spin. The ground spin state of $[Mn^{II}(\mathbf{L^1})_2]$ is high-spin.

Table 2. Nalewajski-Mrozek ("type 3") bond orders calculated at B97-D/TZP and SSB-D/TZP levels of theory on crystal structures of $[Fe^{III}(\mathbf{L^1})_2]^+$ and $[Mn^{II}(\mathbf{L^1})_2]$. Both low spin (LS) and high spin (HS) states are considered.

	$[Fe^{III}(\mathbf{L^1})_2]^+$				$[Mn^{II}(\mathbf{L^1})_2]$[a)]			
DFA	B97-D	B97-D	SSB-D	SSB-D	B97-D	B97-D	SSB-D	SSB-D
Spin-state	LS	HS	LS	HS	LS	HS	LS	HS
M-S1[b)]	0.900	0.592	0.894	0.572	0.751 (0.725)	0.349 (0.362)	0.739 (0.725)	0.335 (0.346)
M-S3	0.906	0.613	0.899	0.592	0.722 (0.766)	0.352 (0.363)	0.716 (0.758)	0.336 (0.350)
M-N4	0.463	0.257	0.451	0.246	0.397 (0.405)	0.158 (0.170)	0.377 (0.390)	0.146 (0.157)
M-N8	0.468	0.264	0.457	0.252	0.403 (0.405)	0.165 (0.163)	0.388 (0.382)	0.152 (0.151)
M-N3	0.544	0.298	0.534	0.283	0.545 (0.473)	0.185 (0.167)	0.525 (0.453)	0.174 (0.157)
M-N7	0.544	0.297	0.534	0.283	0.489 (0.544)	0.173 (0.181)	0.473 (0.520)	0.163 (0.169)

[a)] for Mn(II) complex, two crystallographically independent complexes are considered (X-ray2 in the brackets); [b)]atom numbering is given in **Figs. 1** and **2**.

The most commonly observed coordination polyhedra in hexa-coordinated transition-metal complexes are octahedral (OC-6) and trigonal prismatic (TRP-6). However, one structure very often resembles more than one reference polyhedra. It should be pointed out that Fe(III) complex can be described as a distorted octahedral, while Mn(II) is a distorted trigonal prism. **Table 3** presents the continuous shape measures (CShMs) [65,66], calculated with SHAPE 2.1, to describe deviation from ideal OC-6 and TRP-6 polyhedra for crystal and optimized structures in the ground and excited states. A smaller CShM value indicates that geometry is closer to the reference polyhedron (either OC-6 or TRP-6). **Table 3** reveals that in LS states, OC-6 is the preferred geometry for both complexes. In the HS state, deviation towards TRP-6 is pronounced. The situation is similar in other LS Fe(III) and HS Mn(II) complexes (**Table S14**). It can be seen that departure towards OC-6 geometry makes LS state more stable, as in the case with OPBE DFA, where a minimal energy difference between the ground and excited state can be explained with "wrong" optimized geometry (**Table S12**). SSB-D and B97-D DFAs match the ones from both crystal structures perfectly (**Table 3**, **Tables S11 and S12**). Hence, they are also more reliable for spin-state energetics. OC-6 geometry is also obtained for IS structures (**Table S 15**), albeit more distorted than in the LS cases.

Table 3. Continuous shape measures (CShMs) for $[Fe^{III}(\mathbf{L^1})_2]^+$ and $[Mn^{II}\mathbf{L}_2]$ presenting deviation from ideal OC-6 and TPR-6 polyhedra for crystal and optimized structures at different levels of theory. Both low spin (LS) and high spin (HS) states are considered.

	$[Fe^{III}(\mathbf{L^1})_2]^+$				$[Mn^{II}(\mathbf{L^1})_2]$			
	LS		HS		LS		HS	
	OC-6	TPR-6	OC-6	TPR-6	OC-6	TPR-6	OC-6	TPR-6
X-Ray[a)]	1.731	11.228	--	--	--	--	7.979 (9.974)	6.517 (4.847)

OPBE/TZP	1.556	11.485	4.694	9.097	2.176	11.464	5.926	10.826
OLYP/TZP	1.701	11.489	5.240	8.425	2.328	11.709	6.544	9.273
B97-D/TZP	1.728	12.138	6.334	6.715	2.352	12.689	8.640	6.131
SSB-D/TZP	1.676	11.966	6.681	6.464	2.288	12.769	8.934	6.356
B3LYP*/TZP	1.739	11.484	5.561	7.396	2.458	11.600	6.891	8.303
B97-D/TZP-COSMO[b)]	1.769	12.204	6.432	6.795	2.417	12.342	8.623	6.135
SSB-D/TZP-COSMO[b)]	1.702	12.062	6.825	6.576	2.375	12.147	9.306	5.943

[a)]for Mn(II) complex, two crystallographically independent complexes are considered (X-ray2 in the brackets); [b)]DMSO as solvent.

Since LS and HS complexes usually display different reactivity, we performed further biological tests (see next section). To be sure about the structures of investigated complexes in solution, DFT calculations with the COSMO solvation model have been performed, revealing that geometries remain very similar in the DMSO solution (**Table 3, Tables S11 and S12**). The COSMO calculations did not affect the spin ground states (**Table 1**). Furthermore, these calculations confirm the stability of investigated complexes (**Table S16**).

3.6. Biological activity

The antibacterial activity of the two complexes and their precursors towards a panel of five Gram-negative and five Gram-positive bacteria cells is given in **Table 4**. It can be noticed that the used salts do not show antibacterial activity, while the ligand has activity almost as high as the control antibiotic chloramphenicol. Complexes obtained by complexing the ligand with approximately inactive iron and manganese salts showed antibacterial activity against all tested bacterial strains. The more active complex [Mn(**L**^{1})$_2$] showed very good activity against all tested bacterial cells. The activity of this complex towards *P. hauseri*, *E. coli*, *P. aeruginosa*, *K. pneumoniae*, and *C. sporogenes* was better than that of the control antibiotic. The cationic complex [Fe(**L**^{1})$_2$]$BF_4 \cdot H_2O$ obtained from H**L** and $Fe(BF_4)_2 \cdot 6H_2O$ showed good activity against all tested bacteria but lower than Mn(II) complex. The results of the antifungal activity are given in **Table 5**. Both the ligand and the complexes showed a much weaker activity than the control antifungal agent amphotericin B. Higher activity of the neutral Mn(II) complex can be explained by facilitated transport through the bacterial cell membrane and intracellular dissociation of the complex, which releases the active ligand.

Table 4. Antibacterial activity of tested compounds.

	MIC (mM)						
	H**L**	**1**	**2**	NaN_3	$Fe(BF_4)_2 \cdot 6H_2O$	$MnCl_2 \cdot 4H_2O$	Chloramphenicol
P. hauseri	0.84	0.56	0.17	/	7.41	6.32	0.39
M. luteus	0.42	0.28	0.17	19.23	7.41	6.32	0.10
B. subtilis	0.84	0.28	0.17	38.46	7.41	6.32	0.05
S. aureus	0.84	0.56	0.34	19.23	7.41	6.32	0.05
E. coli	0.84	0.28	0.17	4.81	7.41	12.64	0.19
P. aeruginosa	0.84	0.56	0.17	9.61	7.41	6.32	0.77
K. pneumoniae	0.84	0.56	0.17	/	7.41	12.64	0.19
S. enterica	0.42	0.28	0.34	9.61	7.41	6.32	0.10
C. sporogenes	0.84	0.28	0.17	/	7.41	6.32	0.77
K. rhizophila	0.84	0.56	0.34	19.23	7.41	12.64	0.05

Table 5. Antifungal activity of tested compounds.

	MIC (mM)						
	H**L**[1]	**1**	**2**	NaN_3	$Fe(BF_4)_2{\cdot}6H_2O$	$MnCl_2{\cdot}4H_2O$	Amphotericin B
A. brasiliensis	1.68	1.12	1.37	0.21	7.41	6.32	0.04
C. albicans	0.84	0.56	0.34	0.42	7.41	12.64	0.02
S. cerevisiae	0.84	0.56	0.34	1.68	3.71	6.32	0.01

The results of toxicity of complexes and their precursors against nauplii of *Artemia salina*, as well as radical scavenging activity, are given in **Table 6**. Neither of the tested salts showed significant toxicity, while the cationic complex $[Fe(\mathbf{L^1})_2]BF_4{\cdot}H_2O$ exhibited the highest toxicity. Its toxicity was twice lower than that of the control compound $K_2Cr_2O_7$. The same complex showed the most significant ability to scavenge radicals. The ability of the ion salt to scavenge radicals is preserved in the complexation. DPPH test showed that the ability of the complex $[Fe(\mathbf{L^1})_2]BF_4{\cdot}H_2O$ to scavenge radicals is similar to ascorbic acid. It is likely that the method of complexation and the formation of a cationic complex affects the manifestation of antioxidant activity.

Table 6. Brine shrimp assay and DPPH radical scavenging activity

	Brine shrimp LD_{50} (mM)	DPPH (mM)
H**L**[1]	0.333±0.038	5.544±0.453
1	0.175±0.024	0.262±0.041
2	0.662±0.082	3.874±0.107
NaN_3	0.537±0.078	/
$Fe(BF_4)_2{\times}6H_2O$	1.317±0.104	0.184±0.010
$MnCl_2{\times}4H_2O$	1.406±0.015	/
$K_2Cr_2O_7$	0.077±0.016	/
Ascorbic acid	/	0.079±0.018

4. Conclusions

Complexes **1** and **2** have been synthesized and characterized by X-ray crystallographic analysis, elemental analysis, and IR spectroscopy. In both complexes, the thiosemicarbazone ligand is coordinated in tridentate deprotonated form through the NNS donor set of atoms. The geometry of the six-coordinated Fe(III) ion can be described as distorted octahedral, while Mn(II) ion possesses distorted trigonal-prismatic geometry.

According to the measured effective magnetic moments and DFT studies, the doublet spin state is the ground state for Fe(III) complex. In the case of the Mn(II) complex, the ground state is a sextet with five unpaired electrons. Calculations of spin densities showed that LS states of both complexes have higher bond order than corresponding HS states, and continuous shape measurements revealed that in LS states, OC-6 is the preferred geometry for both complexes. Deviation towards TPR-6 can be noticed and pronounced in the HS state. The more covalent Fe-S bonds, and consequently, the delocalization of electrons, favor an LS state because of the nephelauxetic effect, i.e., smaller pairing energy in Fe(III)

complex. Hund's rule predominates in more ionic Mn(II) complexes, leading to the HS ground spin state.

Investigation of antimicrobial activity showed that upon complexation, both complexes possess higher activity than their precursor compounds. The Mn(II) complex exhibited very good antibacterial activity against all tested bacterial cells, especially towards *P. hauseri*, *E. coli*, *P. aeruginosa*, *K. pneumoniae*, and *C. sporogenes* bacteria. In comparison to Mn(II), Fe(III) complex showed lower activity and, at the same time, higher toxicity (twice lower than the control compound $K_2Cr_2O_7$). The lower activity of the Fe(III) complex can be explained by higher bond order and pronounced covalency of Fe-S bonds.

CRediT authorship contribution statement

M. S., N. S. and M. J. investigation, characterization and writing – original draft; M. Z. and M. G. DFT investigation, writing – review & editing, supervision; A. B., P. P. M. and D. R.; crystallography, writing – original draft; I. N. and D. S. biological investigation; K. A. and B. Č. writing – review & editing.

Declaration of Competing Interest

The authors declare that they have no known competing financial interests or personal relationships that could have appeared to influence the work reported in this paper.

Appendix A. Supplementary data

CCDC 2226697-2226698 contains the supplementary crystallographic data for complexes 1 and 2. These data can be obtained free of charge via http://www.ccdc.cam.ac.uk/conts/retrieving.html, or from the Cambridge Crystallographic Data Centre, 12 Union Road, Cambridge CB2 1EZ, UK; fax: (+44) 1223-336-033; or e-mail: deposit@ccdc.cam.ac.uk.

Supplementary information contains additional crystallographic and computational results, and the Cartesian coordinates of all DFT optimized structures.

Acknowledgements

The authors are grateful to the Ministry of Education, Science and Technological Development of the Republic of Serbia for the financial support (grant numbers: 451-03-68/2022-14/200168, 451-03-68/2022-14/200288 and 451-03-68/2022-14/200026) and The Laboratorio di Strutturistica "M. Nardelli" of the University of Parma and Chiesi Farmaceutici SpA are thanked for the X-ray diffraction data collection. This work has benefited from the equipment and framework of the COMP-HUB Initiative, funded by the

"Departments of Excellence" program of the Italian Ministry for Education, University and Research (MIUR, 2018-2022). This research was supported by the Science Fund of the Republic of Serbia, #7750288, Tailoring Molecular Magnets and Catalysts Based on Transition Metal Complexes – TMMagCat.

References

[1] R. Hoffmann, J.M. Howell, A.R. Rossi, Bicapped tetrahedral, trigonal prismatic, and octahedral alternatives in main and transition group six-coordination, J Am Chem Soc. 98 (1976) 2484–2492. https://doi.org/10.1021/ja00425a016.

[2] M. Zlatar, M. Gruden, Introduction to ligand field theory and computational chemistry, in: Practical Approaches to Biological Inorganic Chemistry, Elsevier, 2020: pp. 17–67. https://doi.org/10.1016/B978-0-444-64225-7.00002-X.

[3] E. Cremades, J. Echeverría, S. Alvarez, The Trigonal Prism in Coordination Chemistry, Chemistry - A European Journal. 16 (2010) 10380–10396. https://doi.org/10.1002/chem.200903032.

[4] M. Costas, J.N. Harvey, Discussion of an open problem, Nat Chem. 5 (2013) 7–9. https://doi.org/10.1038/nchem.1533.

[5] T.S. Lobana, Rekha, R.J. Butcher, A. Castineiras, E. Bermejo, P. v. Bharatam, Bonding Trends of Thiosemicarbazones in Mononuclear and Dinuclear Copper(I) Complexes: Syntheses, Structures, and Theoretical Aspects, Inorg Chem. 45 (2006) 1535–1542. https://doi.org/10.1021/ic051018j.

[6] G. Mahmoudi, A. Castiñeiras, P. Garczarek, A. Bauzá, A.L. Rheingold, V. Kinzhybalo, A. Frontera, Correction: Synthesis, X-ray characterization, DFT calculations and Hirshfeld surface analysis of thiosemicarbazone complexes of M^{n+} ions (n = 2, 3; M = Ni, Cd, Mn, Co and Cu), CrystEngComm. 19 (2017) 1839–1839. https://doi.org/10.1039/C7CE90039B.

[7] P. Bharati, A. Bharti, M.K. Bharty, N.K. Singh, S. Kashyap, U.P. Singh, R.J. Butcher, Cu(II), Zn(II) and Mn(II) complexes of NNS tridentate and Pd(II) complex of NN(μ-S) tetradentate thiobenzyl esters: Synthesis, spectral and X-ray characterization, Polyhedron. 97 (2015) 215–226. https://doi.org/10.1016/j.poly.2015.05.015.

[8] T.S. Lobana, S. Khanna, R.J. Butcher, A.D. Hunter, M. Zeller, Synthesis, crystal structures and multinuclear NMR spectroscopy of copper(I) complexes with benzophenone thiosemicarbazone, Polyhedron. 25 (2006) 2755–2763. https://doi.org/10.1016/j.poly.2006.04.006.

[9] A. Bharti, P. Bharati, N.K. Singh, M.K. Bharty, NNS tridentate thiosemicarbazide and 1,3,4-thiadiazole-2-amine complexes of some transition metal ions: syntheses, structure

and fluorescence properties, J Coord Chem. 69 (2016) 1258–1271. https://doi.org/10.1080/00958972.2016.1160074.

[10] A.E. Stacy, D. Palanimuthu, P. v. Bernhardt, D.S. Kalinowski, P.J. Jansson, D.R. Richardson, Zinc(II)–Thiosemicarbazone Complexes Are Localized to the Lysosomal Compartment Where They Transmetallate with Copper Ions to Induce Cytotoxicity, J Med Chem. 59 (2016) 4965–4984. https://doi.org/10.1021/acs.jmedchem.6b00238.

[11] S.A. Khan, M. Yusuf, Synthesis, spectral studies and in vitro antibacterial activity of steroidal thiosemicarbazone and their palladium (Pd (II)) complexes, Eur J Med Chem. 44 (2009) 2270–2274. https://doi.org/10.1016/j.ejmech.2008.06.008.

[12] G. Pelosi, F. Bisceglie, F. Bignami, P. Ronzi, P. Schiavone, M.C. Re, C. Casoli, E. Pilotti, Antiretroviral Activity of Thiosemicarbazone Metal Complexes, J Med Chem. 53 (2010) 8765–8769. https://doi.org/10.1021/jm1007616.

[13] B. Amritha, O. Manaf, M. Nethaji, A. Sujith, M.R. Prathapachandra Kurup, S. Vasudevan, Mn(II) complex of a di-2-pyridyl ketone-N(4)-substituted thiosemicarbazone: Versatile biological properties and naked-eye detection of Fe2+ and Ru3+ ions, Polyhedron. 178 (2020) 114333. https://doi.org/10.1016/j.poly.2019.114333.

[14] T.T. Adejumo, N. v. Tzouras, L.P. Zorba, D. Radanović, A. Pevec, S. Grubišić, D. Mitić, K.K. Anđelković, G.C. Vougioukalakis, B. Čobeljić, I. Turel, Synthesis, Characterization, Catalytic Activity, and DFT Calculations of Zn(II) Hydrazone Complexes, Molecules. 25 (2020) 4043. https://doi.org/10.3390/molecules25184043.

[15] D. Darmanović, D. Radanović, M. Jevtović, I. Turel, A. Pevec, M. Milčić, M. Gruden, M. Zlatar, N. Đorđević, K. Anđelković, B. Čobeljić, Coordination preferences of NNO and NNS Schiff base ligands with Co(III) complexes: Synthesis, characterization and DFT calculation, J Mol Struct. 1266 (2022) 133509. https://doi.org/10.1016/j.molstruc.2022.133509.

[16] P. v. Bernhardt, J. Mattsson, D.R. Richardson, Complexes of Cytotoxic Chelators from the Dipyridyl Ketone Isonicotinoyl Hydrazone (HPKIH) Analogues, Inorg Chem. 45 (2006) 752–760. https://doi.org/10.1021/ic051573l.

[17] G.M. Sheldrick, SHELXT – Integrated space-group and crystal-structure determination, Acta Crystallogr A Found Adv. 71 (2015) 3–8. https://doi.org/10.1107/S2053273314026370.

[18] G.M. Sheldrick, Crystal structure refinement with SHELXL, Acta Crystallogr C Struct Chem. 71 (2015) 3–8. https://doi.org/10.1107/S2053229614024218.

[19] O. v. Dolomanov, L.J. Bourhis, R.J. Gildea, J.A.K. Howard, H. Puschmann, OLEX2: a complete structure solution, refinement and analysis program, J Appl Crystallogr. 42 (2009) 339–341. https://doi.org/10.1107/S0021889808042726.

[20] G. te Velde, F.M. Bickelhaupt, E.J. Baerends, C. Fonseca Guerra, S.J.A. van Gisbergen, J.G. Snijders, T. Ziegler, Chemistry with ADF, J Comput Chem. 22 (2001) 931–967. https://doi.org/10.1002/jcc.1056.

[21] E.J. Baerends, T. Ziegler, A.J. Atkins, J. Autschbach, D. Bashford, O. Baseggio, A. Bérces, F.M. Bickelhaupt, C. Bo, P.M. Boerritger, L. Cavallo, C. Daul, D.P. Chong, D. v Chulhai, L. Deng, R.M. Dickson, J.M. Dieterich, D.E. Ellis, M. van Faassen, A. Ghysels, A. Giammona, S.J.A. van Gisbergen, A. Goez, A.W. Götz, S. Gusarov, F.E. Harris, P. van den Hoek, Z. Hu, C.R. Jacob, H. Jacobsen, L. Jensen, L. Joubert, J.W. Kaminski, G. van Kessel, C. König, F. Kootstra, A. Kovalenko, M. Krykunov, E. van Lenthe, D.A. McCormack, A. Michalak, M. Mitoraj, S.M. Morton, J. Neugebauer, V.P. Nicu, L. Noodleman, V.P. Osinga, S. Patchkovskii, M. Pavanello, C.A. Peeples, P.H.T. Philipsen, D. Post, C.C. Pye, H. Ramanantoanina, P. Ramos, W. Ravenek, J.I. Rodríguez, P. Ros, R. Rüger, P.R.T. Schipper, D. Schlüns, H. van Schoot, G. Schreckenbach, J.S. Seldenthuis, M. Seth, J.G. Snijders, M. Solà, S. M., M. Swart, D. Swerhone, G. te Velde, V. Tognetti, P. Vernooijs, L. Versluis, L. Visscher, O. Visser, F. Wang, T.A. Wesolowski, E.M. van Wezenbeek, G. Wiesenekker, S.K. Wolff, T.K. Woo, A.L. Yakovlev, ADF 2022.1, SCM, Theoretical Chemistry, Vrije Universiteit, Amsterdam, The Netherlands, https://www.scm.com, (n.d.).

[22] R. Rüger, M. Franchini, T. Trnka, A. Yakovlev, E. van Lenthe, P. Philipsen, T. van Vuren, B. Klumpers, T. Soini, AMS 2022.1, SCM, Theoretical Chemistry, Vrije Universiteit, Amsterdam, The Netherlands, http://www.scm.com, (n.d.).

[23] E. van Lenthe, E.J. Baerends, J.G. Snijders, Relativistic regular two-component Hamiltonians, J Chem Phys. 99 (1993) 4597–4610. https://doi.org/10.1063/1.466059.

[24] A.D. Becke, Density-functional exchange-energy approximation with correct asymptotic behavior, Phys Rev A (Coll Park). 38 (1988) 3098–3100. https://doi.org/10.1103/PhysRevA.38.3098.

[25] J.P. Perdew, Density-functional approximation for the correlation energy of the inhomogeneous electron gas, Phys Rev B. 33 (1986) 8822–8824. https://doi.org/10.1103/PhysRevB.33.8822.

[26] J.P. Perdew, Erratum: Density-functional approximation for the correlation energy of the inhomogeneous electron gas, Phys Rev B. 34 (1986) 7406–7406. https://doi.org/10.1103/PhysRevB.34.7406.

[27] S. Grimme, J. Antony, S. Ehrlich, H. Krieg, A consistent and accurate ab initio parametrization of density functional dispersion correction (DFT-D) for the 94 elements H-Pu., J Chem Phys. 132 (2010) 154104. https://doi.org/10.1063/1.3382344.

[28] S. Grimme, S. Ehrlich, L. Goerigk, Effect of the damping function in dispersion corrected density functional theory., J Comput Chem. 32 (2011) 1456–1465. https://doi.org/10.1002/jcc.21759.

[29] E. Bitzek, P. Koskinen, F. Gähler, M. Moseler, P. Gumbsch, Structural relaxation made simple, Phys Rev Lett. 97 (2006) 170201. https://doi.org/10.1103/PHYSREVLETT.97.170201/FIGURES/2/MEDIUM.

[30] M. Swart, A.W. Ehlers, K. Lammertsma, Performance of the OPBE exchange-correlation functional, Mol Phys. 102 (2004) 2467–2474. https://doi.org/10.1080/00268970420002750 17.

[31] N.C. Handy, A.J. Cohen, Left-right correlation energy, Mol Phys. 99 (2001) 403–412. https://doi.org/10.1080/00268970010018431.

[32] C. Lee, W. Yang, R.G. Parr, Development of the Colle-Salvetti correlation-energy formula into a functional of the electron density, Phys Rev B. 37 (1988) 785–789. https://doi.org/10.1103/PhysRevB.37.785.

[33] B.G. Johnson, P.M.W. Gill, J.A. Pople, The performance of a family of density functional methods, J Chem Phys. 98 (1993) 5612. https://doi.org/10.1063/1.464906.

[34] T. v. Russo, R.L. Martin, P.J. Hay, Density functional calculations on first-row transition metals, J Chem Phys. 101 (1994) 7729. https://doi.org/10.1063/1.468265.

[35] S. Grimme, Semiempirical GGA-type density functional constructed with a long-range dispersion correction., J Comput Chem. 27 (2006) 1787–99. https://doi.org/10.1002/jcc.20495.

[36] M. Swart, M. Solà, F.M. Bickelhaupt, A new all-round density functional based on spin states and S(N)2 barriers., J Chem Phys. 131 (2009) 094103. https://doi.org/10.1063/1.3213193.

[37] M. Reiher, O. Salomon, B. Artur Hess, Reparameterization of hybrid functionals based on energy differences of states of different multiplicity, Theoretical Chemistry Accounts: Theory, Computation, and Modeling (Theoretica Chimica Acta). 107 (2001) 48–55. https://doi.org/10.1007/s00214-001-0300-3.

[38] M.A.L. Marques, M.J.T. Oliveira, T. Burnus, Libxc: A library of exchange and correlation functionals for density functional theory, Comput Phys Commun. 183 (2012) 2272–2281. https://doi.org/10.1016/j.cpc.2012.05.007.

[39] M. Swart, F.M. Bickelhaupt, Optimization of strong and weak coordinates, Int J Quantum Chem. 106 (2006) 2536–2544. https://doi.org/10.1002/QUA.21049.

[40] A. Michalak, R.L. Dekock, T. Ziegler, Bond Multiplicity in Transition-Metal Complexes: Applications of Two-Electron Valence Indices, Journal of Physical Chemistry A. 112 (2008) 7256–7263. https://doi.org/10.1021/JP800139G.

[41] A. Klamt, G. Schoermann, COSMO: a new approach to dielectric screening in solvents with explicit expressions for the screening energy and its gradient, Journal of the Chemical Society, Perkin Transactions 2. (1993) 799–805. https://doi.org/10.1039/p29930000799.

[42] A. Klamt, Conductor-like Screening Model for Real Solvents: A New Approach to the Quantitative Calculation of Solvation Phenomena, J Phys Chem. 99 (1995) 2224–2235. https://doi.org/10.1021/j100007a062.

[43] C.C. Pye, T. Ziegler, An implementation of the conductor-like screening model of solvation within the Amsterdam density functional package, Theoretical Chemistry Accounts: Theory, Computation, and Modeling (Theoretica Chimica Acta). 101 (1999) 396–408. https://doi.org/10.1007/s002140050457.

[44] National Committee for Clinical Laboratory Standards, Approval Standard Document M7-A5, Villanova, Pa, USA (2000)., National Committee for Clinical Laboratory Standards, Approval Standard Document M7-A5, Villanova, PA, USA. (2000).

[45] A. Sartoratto, A.L.M. Machado, C. Delarmelina, G.M. Figueira, M.C.T. Duarte, V.L.G. Rehder, Composition and antimicrobial activity of essential oils from aromatic plants used in Brazil, Brazilian Journal of Microbiology. 35 (2004) 275–280. https://doi.org/10.1590/S1517-83822004000300001.

[46] M.S. Blois, Antioxidant Determinations by the Use of a Stable Free Radical, Nature. 181 (1958) 1199–1200. https://doi.org/10.1038/1811199a0.

[47] R.J. Laverick, A.B. Carter, H.A. Klein, A.J. Fitzpatrick, T.D. Keene, G.G. Morgan, J.A. Kitchen, Synthesis and characterisation of Fe(III) and Co(III) complexes of thiazole-containing thiosemicarbazone ligands, Inorganica Chim Acta. 463 (2017) 126–133. https://doi.org/10.1016/j.ica.2017.04.008.

[48] A.B. Carter, R.J. Laverick, D.J. Wales, S.O. Akponasa, A.J. Scott, T.D. Keene, J.A. Kitchen, Investigating the Structure Directing Properties of Designer 1,8-Naphthalimide and Amphiphilic Sulfonate Anions and Their Fe ^{III} Thiosemicarbazone Complexes, Cryst Growth Des. 17 (2017) 5129–5144. https://doi.org/10.1021/acs.cgd.7b00534.

[49] B. Čobeljić, I. Turel, A. Pevec, Z. Jagličić, D. Radanović, K. Anđelković, M.R. Milenković, Synthesis, structures and magnetic properties of octahedral Co(III) complexes of heteroaromatic hydrazones with tetraisothiocyanato Co(II) anions, Polyhedron. 155 (2018) 425–432. https://doi.org/10.1016/j.poly.2018.08.070.

[50] K.R. Dymock, G.J. Palenik, Twist angle calculations. Fact or fantasy, Inorg Chem. 14 (1975) 1220–1222. https://doi.org/10.1021/ic50147a056.

[51] L.J. Farrugia, WinGX and ORTEP for Windows : an update, J Appl Crystallogr. 45 (2012) 849–854. https://doi.org/10.1107/S0021889812029111.

[52] C.F. Macrae, P.R. Edgington, P. McCabe, E. Pidcock, G.P. Shields, R. Taylor, M. Towler, J. van de Streek, Mercury: visualization and analysis of crystal structures, J Appl Crystallogr. 39 (2006) 453–457. https://doi.org/10.1107/S002188980600731X.

[53] D.X. West, J.K. Swearingen, J. Valdés-Martínez, S. Hernández-Ortega, A.K. El-Sawaf, F. van Meurs, A. Castiñeiras, I. Garcia, E. Bermejo, Spectral and structural studies of

iron(III), cobalt(II,III) and nickel(II) complexes of 2-pyridineformamide N(4)-methylthiosemicarbazone, Polyhedron. 18 (1999) 2919–2929. https://doi.org/10.1016/S0277-5387(99)00210-7.

[54] N.C. Saha, A. Saha, R.J. Butcher, S. Chaudhuri, N. Saha, Synthesis and structural characterisation of new iron(III) complexes with biologically relevant pyrazolyl thiosemicarbazones, Inorganica Chim Acta. 339 (2002) 348–354. https://doi.org/10.1016/S0020-1693(02)00935-0.

[55] N.C. Saha, R.J. Butcher, S. Chaudhuri, N. Saha, Synthesis and spectroscopic studies of cobalt(III) complexes with 5-methyl-3-formylpyrazole-N(4)-diethylthiosemicarbazone (HMPzNEt2): X-ray crystallography of [Co(MPzNEt2)2]ClO4·2H2O (I) and [Co(MPzNEt2)2]BF4·2H2O (II), Polyhedron. 21 (2002) 779–785. https://doi.org/10.1016/S0277-5387(02)00847-1.

[56] N.C. Saha, R.J. Butcher, S. Chaudhuri, N. Saha, Synthesis and spectroscopic identification of new iron(III) complexes with 5-methyl-3-formylpyrazole-3-piperidinylthiosemicarbazone (HMPz3Pi): X-ray structure of [Fe(MPz3Pi)2]ClO4·2H2O, Polyhedron. 22 (2003) 375–381. https://doi.org/10.1016/S0277-5387(02)01342-6.

[57] A. Sreekanth, M.R.P. Kurup, Synthesis, EPR and Mössbauer spectral studies of new iron(III) complexes with 2-benzoylpyridine-N(4), N(4)-(butane-1,4-diyl) thiosemicarbazone (HBpypTsc): X-ray structure of [Fe(BpypTsc)2]FeCl4·2H2O and the free ligand, Polyhedron. 23 (2004) 969–978. https://doi.org/10.1016/j.poly.2004.01.006.

[58] C.G. Oliveira, P.I. da S. Maia, P.C. Souza, F.R. Pavan, C.Q.F. Leite, R.B. Viana, A.A. Batista, O.R. Nascimento, V.M. Deflon, Manganese(II) complexes with thiosemicarbazones as potential anti-Mycobacterium tuberculosis agents, J Inorg Biochem. 132 (2014) 21–29. https://doi.org/10.1016/j.jinorgbio.2013.10.011.

[59] A. Sreekanth, M. Joseph, H.-K. Fun, M.R.P. Kurup, Formation of manganese(II) complexes of substituted thiosemicarbazones derived from 2-benzoylpyridine: Structural and spectroscopic studies, Polyhedron. 25 (2006) 1408–1414. https://doi.org/10.1016/j.poly.2005.10.004.

[60] V. Philip, V. Suni, M.R.P. Kurup, M. Nethaji, Manganese(II) complexes of substituted di-2-pyridyl ketone thiosemicarbazones: Structural and spectral studies, Spectrochim Acta A Mol Biomol Spectrosc. 64 (2006) 171–177. https://doi.org/10.1016/j.saa.2005.07.013.

[61] P.F. Rapheal, E. Manoj, M.R.P. Kurup, Syntheses and EPR spectral studies of manganese(II) complexes derived from pyridine-2-carbaldehyde based N(4)-substituted thiosemicarbazones: Crystal structure of one complex, Polyhedron. 26 (2007) 5088–5094. https://doi.org/10.1016/j.poly.2007.07.028.

[62] M. Swart, M. Gruden, Spinning around in Transition-Metal Chemistry, Acc Chem Res. 49 (2016) 2690–2697. https://doi.org/10.1021/acs.accounts.6b00271.

[63] M. Zlatar, M. Gruden, Introduction to ligand field theory and computational chemistry, in: R.R. Crichton, R.O. Louro (Eds.), Practical Approaches to Biological Inorganic Chemistry, 2nd ed., Elsevier, 2020: pp. 17–67. https://doi.org/10.1016/B978-0-444-64225-7.00002-X.

[64] M. Swart, Accurate Spin-State Energies for Iron Complexes, J Chem Theory Comput. 4 (2008) 2057–2066. https://doi.org/10.1021/ct800277a.

[65] M. Pinsky, D. Avnir, Continuous symmetry measures. 5. The classical polyhedra, 37 (1998) 5575–5582. https://doi.org/10.1021/IC9804925.

[66] S. Alvarez, P. Alemany, D. Casanova, J. Cirera, M. Llunell, D. Avnir, Shape maps and polyhedral interconversion paths in transition metal chemistry, Coord Chem Rev. 249 (2005) 1693–1708. https://doi.org/10.1016/J.CCR.2005.03.031.